universe

IMPACT FACTOR 2.9

CITESCORE 3.6

Article

Studying the Spectral Energy Distributions Emanating from Regular Galactic XRBs

Theodora Papavasileiou, Odysseas Kosmas and Ioannis Sinatkas

MDPI

https://doi.org/10.3390/universe9070312

universe

MDPI

Article

Studying the Spectral Energy Distributions Emanating from Regular Galactic XRBs

Theodora Papavasileiou [1,2,*], Odysseas Kosmas [1,3] and Ioannis Sinatkas [2]

[1] Department of Physics, University of Ioannina, GR-45110 Ioannina, Greece; odykosm@gmail.com
[2] Department of Informatics, University of Western Macedonia, GR-52100 Kastoria, Greece; isinatkas@uowm.gr
[3] Conigital LTD, 51 Parkside, Coventry CV1 2HG, UK
* Correspondence: th.papavasileiou@uowm.gr

Abstract: X-ray binary systems (XRBs) exhibit similar dynamics and multimessenger emission mechanisms to active galactic nuclei (AGNs) with the benefit of shorter time scaling. Those systems produce rich spectral energy distributions (SEDs) ranging from the radio band to the very high energy gamma rays. The emission origin varies between the system's accretion disk (X-rays) to the corona and, most notably, to the two twin plasma ejections (jets) that often meet the interstellar medium forming highly observable radio lobes. Modeling of the jets offers an excellent opportunity to understand the intrinsic mechanisms and the jet particles, such as electrons, positrons, and protons. In this work, we employ a lepto-hadronic jet model that assumes particle acceleration through shock waves over separate zonal regions of the jet. The hadronic models consider proton–proton collisions that end up in gamma-ray photons through neutral pion decays. The main leptonic mechanisms involve synchrotron radiation (from both electrons and protons) and inverse Compton scattering of ambient photons (coming from the disk, the corona, and the companion star) on jet electrons. The emissions from the disk, the corona, and the donor star are also included in the SED calculations, along with the photon absorption effects due to their interaction with higher-energy jet photons. We apply the model on a $10M_{\odot}$ black hole accreting at the Eddington rate out of a $20M_{\odot}$ companion star. One of our goals is to investigate and determine an optimal frame concerning the values for the free parameters that enter our calculations to produce higher integral fluxes.

Keywords: XRBs; lepto-hadronic jet; accretion disk; radiation absorption; gamma rays; SEDs; inverse Compton scattering; synchrotron emission

Citation: Papavasileiou, T.; Kosmas, O.; Sinatkas, I. Studying the Spectral Energy Distributions Emanating from Regular Galactic XRBs. *Universe* **2023**, *9*, 312. https://doi.org/10.3390/universe9070312

Academic Editor: Pat Romano

Received: 28 March 2023
Revised: 18 June 2023
Accepted: 19 June 2023
Published: 28 June 2023

1. Introduction

The twin jets associated with the radio emission emanating from black hole X-ray binaries (BHXRBs) have attracted many researchers dealing with the variety of the energy-exchanging mechanisms they present, the relativistic magnetohydrodynamical nature, and the leading forces hidden behind these ejections as well as the jet collimation. A magnetically led process of field lines attached to the accretion disk, collecting ambient particles to be collimated and accelerated perpendicularly to the disk's plane, was proposed long ago [1]. The particles' nature is still unclear, although the leading beliefs include pair (e^+e^-) or electron/proton-dominated jets. Lepton-induced emission mechanisms, such as synchrotron radiation and Compton up-scattering, are further considered in explaining the jet-produced spectra of energies up to a few GeVs [2–8].

On the other hand, hadronic models have been proven helpful in predicting very high energy (VHE) gamma rays and neutrinos from the jet blobs [9–11]. A combination of both, however, may be considered optimized treatment in our attempt to predict the spectral energy distribution (SED) of the wide frequency band covering the low radio frequency up to the VHE gamma-ray emission (i.e., 10^{-13}–10^{8} GeV).

The accretion disk, depending on the temperature at its innermost heated regions [12,13], is a constant source of soft or hard X-rays. The most common disk model is the so-called

Shakura–Sunyaev [14], describing a thin accretion disk with high optical thickness in the equatorial region of stellar mass or supermassive black holes accreting near the Eddington limit. Furthermore, there are accretion solutions describing a low-density infalling gas that radiates a minimum portion of its energy (<1%). This radiatively inefficient accretion flow type is called advection-dominated (ADAF) [15]. In this work, we adopt the assumption of a classic Shakura–Sunyaev disk, which is heated mainly through viscous dissipation. The inner disk boundary is often placed at the last stable orbital radius, which depends on the rotational state of the black hole [16].

The jet model assumes a conic-like lepto-hadronic plasma, collimated and accelerated by the magnetic field lines [5,11]. In our case, the energy responsible for the jet confinement is considered equal to the plasma kinetic energy [11]. Moreover, a portion of the jet lepto-hadrons, distinguished by the free parameter q_{rel}, are further accelerated due to shock waves. That process takes place within a jet length located at a distance of z_0 to z_{max} (with $z_{max} = jz_0$) from the black hole. The relativistic jet content participates in various energy-altering interactions with the magnetic field lines, slower particles, or photons produced inside or outside the jet boundaries (i.e., synchrotron, inverse Compton, synchrotron self-Compton, $p - p$, $p - \gamma$, etc.); see Refs. [17–19] and references therein. The corresponding broadband emission covers the spectrum from radio to very high energy (VHE) gamma rays. Although many X-ray binaries (XRBs) have been observed in X-ray and radio frequencies, VHE gamma-ray emissions have been rarely recorded from these astrophysical systems except for a few distinguished cases, such as LS 5039 [20]. We attempt to shed some light on the aforementioned open issues by assuming photon absorption effects due to emission from the highly heated accretion disk and the supergiant companion star. Additionally, coronal contributions are also significant in explaining partly the observed hard X-ray emission coming from XRBs [21].

The model is applied on a standard black hole X-ray binary system, namely, a system whose characteristics (i.e., stellar masses, companion stellar type, accretion disk size, orbital period, etc.) do not deviate from the scale of the well-studied XRBs, such as Cygnus X-1 and GRS 1915+105. Hence, a standard XRB, in our case, is a $10M_\odot$ black hole in rotation with a $20M_\odot$ O-type supergiant companion star with an orbital period of $P_{orb} \approx 6$ days. The binary's distance to the Earth is assumed to be $d = 2$ kpc, and the inclination to the line of sight is $i = 20^\circ$, presenting a better view of the well-collimated incoming jet with a half-opening angle of $\xi = 2^\circ$. In addition, the mass accretion rate falls in the Eddington limit, justifying the implementation of the Shakura–Sunyaev disk model. The jet's bulk velocity is considered to reach 90% of the speed of light.

In the following sections, we describe the contribution of the accretion disk to the total SED in addition to the total optical thickness of the photon cloud interacting with a single jet photon while traveling to the observer (Section 2). Then, we make a similar analysis regarding the companion star of our model XRB (Section 3). The jet dynamics are described in Section 4 in two subsections corresponding to the lepton- and hadron-induced dominant mechanisms. Finally, we present and discuss our findings in Section 5 and summarize our conclusions in Section 6.

2. Accretion Disk Luminosity

Fueled by the accretion process, the disk emits effectively in the X-ray band. The emitted luminosity depends on the mass accretion rate $\dot{M}_{accr}$, which is related to the temperature at its innermost parts as [22]

$$T_{max} = \left(\frac{3GM_{BH}\dot{M}_{accr}}{8\pi\sigma_{SB}R_g^3} \right)^{1/4}. \quad (1)$$

Here, σ_{SB} is the Stefan–Boltzmann constant, and R_g the respective gravitational radius ($R_g = R_{Sch}/2$). In many BHXRBs, the total disk luminosity does not exceed the Eddington limit $L_{disk} \approx 10^{38}$ erg/s, corresponding to a mass accretion rate of $\dot{M}_{accr} = 10^{-8}\ M_\odot/\mathrm{yr}$.

This is also the value employed here, assuming a regular BHXRB that does not present any unique characteristic or nonordinary geometry.

A single radial surface element of the disk emits a black-body spectrum described by assuming thermal equilibrium

$$\frac{dn}{d\epsilon d\Omega} = \frac{2}{h^3c^3}\frac{\epsilon^2}{e^{\epsilon/k_BT(R)}-1}. \tag{2}$$

The temperature's dependence on the disk radius is given by [23]

$$T(R) = T_{max}\left[\frac{R/R_g - 2/3}{R/R_g(R/R_g-2)^3}\left(1-\frac{3^{3/2}(R/R_g-2)}{2^{1/2}(R/R_g)^{3/2}}\right)\right]^{1/4}. \tag{3}$$

After integrating over the disk's solid angle, assuming it begins at $R_{in} = 6R_g$ (i.e., with $M_{BH} = 10M_\odot$), the emitted luminosity per energy unit is estimated to be

$$L = 4\pi D^2 c\epsilon^2 \frac{dn}{d\epsilon}, \tag{4}$$

where we implement a distance D that approximates the binary system's distance to the Earth and is much greater than the disk's radius (i.e., $D \approx d \gg R$).

Furthermore, the disk photons eliminate mostly the high-energy photons originating from the system's jet, leading to pair production. The calculation of the respective optical depth requires integration over the disk's solid angle $d\Omega$, high-energy photon path towards the observer l, and disk photon energy ϵ

$$\tau_{disk} = \int_0^\infty \int_0^{2\pi} \int_{R_{in}}^{R_{out}} \int_{\epsilon_{min}}^\infty \frac{dn}{d\epsilon d\Omega}(1-\cos\theta_0) \times \sigma_{\gamma\gamma}\frac{\rho\cos\omega}{D^3} R dR d\phi d\epsilon dl. \tag{5}$$

The energy integration limit is $\epsilon_{min} = 2m_e^2c^4/E_{ph}(1-\cos\theta_0)$ with E_{ph} being the jet photon energy, θ_0 is the angle between the two interacting photons, ρ is the distance between the interaction point and the center of the black hole, D is the corresponding distance from the emitting disk surface element, and ω is the angle between ρ and the ejection axis z. A detailed geometrical analysis can be found in [23]. We mention that the angle θ_0 depends on several of the aforementioned geometrical aspects, such as the system inclination i, the photon path's length l, the disk's solid angle Ω, and D and ρ.

The pair production cross-section $\sigma_{\gamma\gamma}$ of Equation (5) is given by [24]

$$\sigma_{\gamma\gamma}(E_{ph},\epsilon,\theta_0) = \frac{\pi e^4}{2m^2c^4}\left(1-\beta^2\right) \times \left[\left(3-\beta^4\right)ln\left(\frac{1+\beta}{1-\beta}\right) - 2\beta\left(2-\beta^2\right)\right], \tag{6}$$

where $\beta = \sqrt{1-\frac{1}{\mu}}$. For the production of an electron–positron pair, it must hold $\mu > 1$, where $\mu = \epsilon E_{ph}(1-\cos\theta_0)/2m^2c^4$.

In the left panel of Figure 1, we plot the optical depth at the distance $z = 10^8$ cm ($\approx 68R_g$ with $M_{BH} = 10M_\odot$) as a function of the energy E for three values of the outer disk radius R_{out}, where the contribution of the extended surface is assessed. A donor star that fills 90% of its Roche lobe is associated with an accretion disk of $R_{out} \approx 10^{12}$ cm. However, beyond $R_{out} = 10^9$ cm, pair production severely diminishes. The right panel of Figure 1 presents the total disk luminosity given by Equation (4) as a function of E for distinct values of the mass accretion rate and outer disk radius R_{out}. Note that super-Eddington accretion rates extend the emission spectrum up to the hard X-ray band.

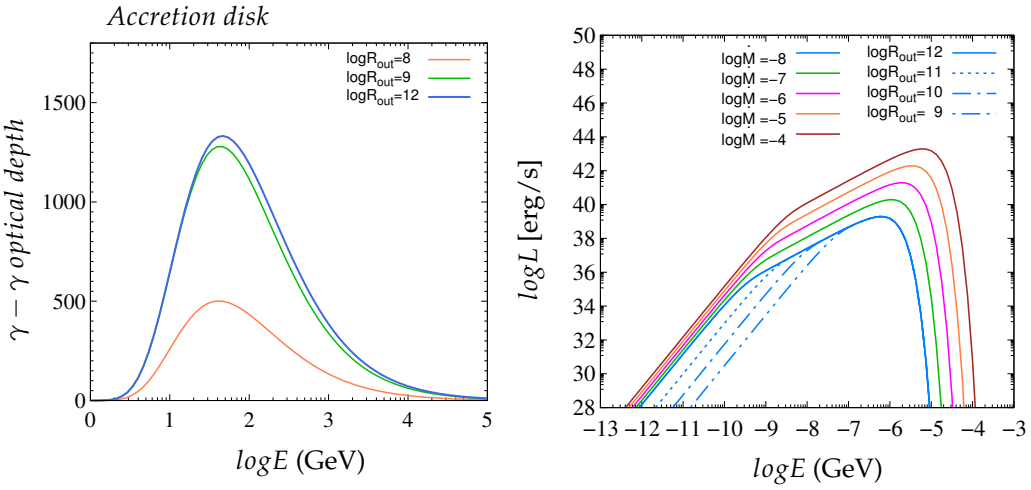

Figure 1. Optical depth for pair production at the distance $z = 10^8$ cm ($\approx 68R_g$ with $M_{BH} = 10M_\odot$) (**left panel**) and luminosity (**right panel**) attributed to the accretion disk for varying disk sizes (in cm) and mass accretion rates (in $M_\odot$/yr).

3. Secondary Stellar Component

We assume a supergiant secondary star of type O, similar to HDE 226868 of Cygnus X-1, that constitutes an adequate source of UV emission (1–30 eV) with a spectrum described by [25]

$$\frac{dn}{d\epsilon} = \frac{15}{4\pi^5 c} \frac{L_* \epsilon^2}{D^2 (k_B T_*)^4 \left(e^{\epsilon/k_B T_*} - 1\right)}, \tag{7}$$

where L_* and T_* are the total stellar luminosity and effective surface temperature, respectively. D is the distance from the star. In the case of photon annihilation with jet photons, D involves the distance z of the emission region from the black hole, the distance covered by the emitted jet photon, the binary separation of the system (i.e., the distance between the two stellar components), the angle of the jet to the line of sight, and the orbital phase ϕ. The binary separation is often of the order of $s \approx 10^{12}$ cm, which, in most cases, dictates the scale of D.

The optical thickness of the emitted photon cloud, as seen by a single jet-emitted photon while traveling towards the Earth, is defined by [25]

$$\tau_{donor} = \int_0^{+\infty} \int_{\epsilon_{min}}^{+\infty} \frac{dn}{d\epsilon} (1 - \cos\theta_0) \sigma_{\gamma\gamma} d\epsilon dl, \tag{8}$$

where $\epsilon_{min} = 2m_e^2 c^4 / E_{ph}(1 - \cos\theta_0)$. The angle θ_0 between the interacting photons depends on the distances l, z, and s and angles i along with ϕ.

In Figure 2, we demonstrate, similarly to the accretion disk case, the estimated optical depth (for the same distance of $z = 10^8$ cm) (left panel) and the emitted luminosity (right panel). The optical depth grows 3–4 times from its lowest point corresponding to a star eclipsed by the BH (i.e., $\phi = \pi$), assuming a nearly circular orbit (with no eccentricity). However, the orbital phase transition between the moments of emission and the photon encounter is often negligible (i.e., $\Delta\phi \approx 0$).

Finally, concerning the stellar luminosity estimation in the right panel of Figure 2, we assume temperatures corresponding to the supergiant class hypothesis and notice only a spectrum shift, which is expected since the total stellar luminosity is constant, $L_* = 10^4 L_\odot$ (see Table 1).

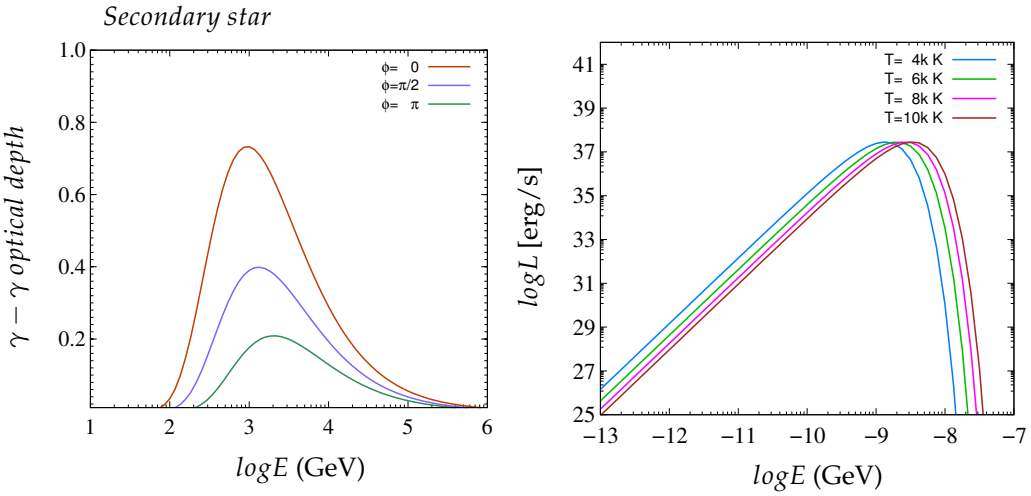

Figure 2. The optical thickness of the secondary star's emission τ_{donor} as seen by a passing photon (left panel) and stellar luminosity (right panel) corresponding to different orbital phases and effective surface temperatures, respectively. The photon is emitted from a jet region at the distance $z = 10^8$ cm ($\approx 68 R_g$ with $M_{BH} = 10 M_\odot$) from the black hole.

Table 1. Standard values of the free parameters and the parameters of the studied X-ray binary (XRB) employed in the model application.

Free Parameter	**Symbol**	**Value**	**Units**
Acceleration efficiency	η	0.1	-
Jet portion of relativistic matter	q_{rel}	10^{-4}	-
Hadron to lepton ratio	α	1	-
Acceleration zone length factor	j	5	-
Acceleration region start	z_0	10^{12}	cm
XRB Parameter	**Symbol**	**Value**	**Units**
Black hole mass	M_{BH}	10	$M_\odot$
Secondary stellar mass	M_*	20	$M_\odot$
Distance to Earth	d	2	kpc
Orbital period	P_{orb}	6	days
Stellar luminosity	L_*	10^4	$L_\odot$
Stellar temperature	T_*	10^4	K
Initial secondary stellar phase	ϕ	0	$^\circ$
XRB inclination	i	20	$^\circ$
Jet bulk velocity	β_b	0.9	c
Jet Lorentz factor	Γ_b	2.29	-
Magnetic field strength	$B(z_0)$	5.5×10^3	G
Jet's half-opening angle	ξ	2	$^\circ$
Mass accretion rate	$\dot{M}_{accr}$	10^{-8}	$M_\odot$/yr
Disk maximum temperature	T_{max}	2.72×10^7	K
Disk innermost radius	R_{in}	8.88×10^6	cm
Disk outermost radius	R_{out}	1.22×10^{12}	cm
Binary separation	s	4.22×10^{12}	cm

4. Jet Emission

The investigation of the produced SEDs begins with the energy distributions of the primary particles (leptons and/or hadrons). They stem from the combination of the energy-gain and energy-loss processes inside the jet, including shock-induced acceleration in the first case and synchrotron radiation, inverse comptonization, and collisions, regarding energy losses [26]. The acceleration mechanism follows a power-law description of the

primary particles' production rate. The assumed steady-state transfer equation is written as

$$\frac{\partial N(E,z)b(E,z)}{\partial E} + t^{-1}N(E,z) = Q(E,z)\,, \tag{9}$$

where $b(E,z)$ represents the energy-loss rate . The second term on the left-hand side includes the particles' density reduction due to abandoning the jet frame or particle (pions, muons, etc.) decaying. The injection function (or production rate) is given as a transformation product in the observer's rest frame

$$Q(E,z) = Q_0\left(\frac{z_0}{z}\right)^3 \frac{\Gamma_b^{-1}\left(E - \beta_b \cos i\sqrt{E^2 - m^2c^4}\right)^{-2}}{\sqrt{\sin^2 i + \Gamma_b^2\left(\cos i - \frac{\beta_b E}{\sqrt{E^2 - m^2c^4}}\right)^2}}\,, \tag{10}$$

where z_0 is the starting point of the acceleration, Γ_b is the Lorentz factor, and $v_b = \beta_b$c. We assume the acceleration zone (i.e., starting from z_0) to be located farther away from the jet's base (i.e., $z_b \approx 10^7$ cm), where it is not affected by the jet launching dynamics. The angle i dictates the inclination angle (see Figure 3). Q_0 is the normalization constant attributed separately to protons and electrons based on their total luminosity. They are given based on the total luminosity of the relativistic particles $L_{rel} = q_{rel}L_{kin}$, which splits between the protons and electrons according to a free parameter as $L_{rel} = L_p + L_e = (\alpha + 1)L_e$. Hence, we have $L_e = q_{rel}L_{kin}/(\alpha + 1)$ and $L_p = \alpha L_e$. The value of α indicates whether the model inclines towards leptonic ($\alpha \approx 0$) or hadronic jet description ($\alpha \gg 1$).

In general, the magnetic field strength, defined as

$$B(z) = \left(\frac{8L_{kin}}{v_b R_{jet}^2}\right)^{1/2}\,, \tag{11}$$

is determined by assuming the magnetic energy density to be equal to the plasma counterpart (i.e., $L_B \approx L_{kin}$). The latter is distributed among the electrons and protons inside the jet. The magnetic field strength at the base of the jet is of the order of $B \approx 10^7$ G, which is also supported by theoretical predictions [27,28].

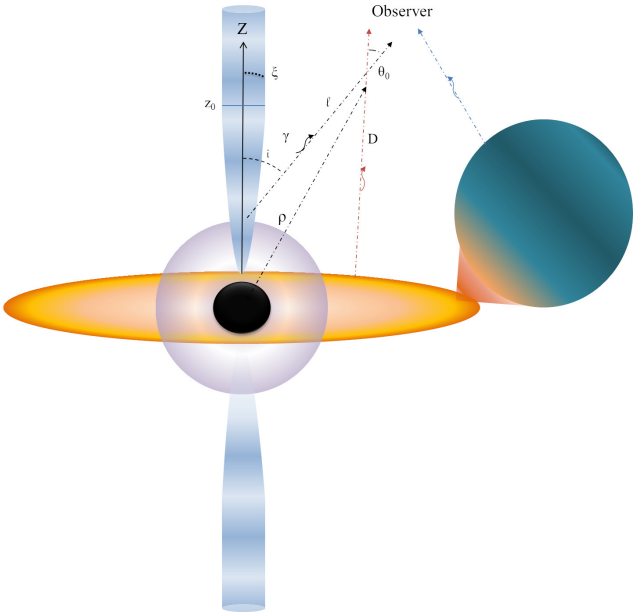

Figure 3. A black hole X-ray binary representation featuring the main emission components that contribute to the respective spectral energy distribution (SED).

4.1. Leptonic Mechanisms

4.1.1. Synchrotron Emission

Synchrotron radiation emission results from the magnetically induced acceleration of relativistic charged particles, such as electrons and protons. However, it is mainly an electron-implicated mechanism. In the present work, we will also take into account the synchrotron radiation emitted by the jet protons.

The power spectrum emitted by a single electron (or proton) accelerated by a magnetic field $B(z)$ is written as [2]

$$P_{syn}(E_{ph}, E, z, \alpha) = \frac{\sqrt{3}e^3 B(z)}{hmc^2} \frac{E_{ph}}{E_{cr}} \int_{E_{ph}/E_{cr}}^{\infty} K_{5/3}(\zeta) d\zeta \,, \tag{12}$$

with the respective critical energy E_{cr} defined as

$$E_{cr} = \frac{3heB(z) \sin \alpha_p}{4\pi mc} \gamma^2 \,. \tag{13}$$

The pitch angle is represented by a_p and $\gamma = E/mc^2$. The total power per energy unit that is radiated by a distribution of particles is obtained by the integration over the solid angle associated with the pitch angle and particle energy as

$$q_{syn}(E_{ph}, z) = \int d\Omega_{\alpha_p} \int_{E_{e,p}^{(min)}}^{E_{e,p}^{(max)}} P_{syn} N_{e,p}(E, z) dE \,. \tag{14}$$

The corresponding synchrotron luminosity is given by

$$L_{syn}^{(e,p)}(E_{ph}) = \int_V d^3 r E_{ph} q_{syn}^{(e,p)} \,, \tag{15}$$

where the integration takes place over the conic jet volume of the acceleration zone.

4.1.2. Inverse Comptonization

Photons emitted by the accretion disk, the corona, and the donor star participate in inverse Compton interactions with highly energetic electrons of the jet or the pair products of $\gamma - \gamma$ interactions in addition to the corona particles. Our study assumes isotropic photon densities from the accretion disk, the donor star , and the corona, gaining energy from the accelerated jet leptons. The energies involved belong to both the Thomson and the Klein–Nishina regime.

The scattered photon spectrum produced by a single electron is given by [2]

$$q_{IC}(\epsilon, E, E_{ph}) = \frac{3\sigma_T m^2 c^5}{4\gamma} \frac{dn}{\epsilon d\epsilon} [2f ln f + (1 + 2f)(1 - f) + F] \,, \tag{16}$$

where $\gamma \gg 1$, σ_T denotes the known Thomson cross-section and the dimensionless parameter $f = E_{ph} E / 4\epsilon\gamma^2 (E - E_{ph})$. Additionally, it holds

$$F = \frac{k^2(1 - f)}{2(1 + k)} \,, \tag{17}$$

where $k = E_{ph}/(E - E_{ph})$. The total spectrum is obtained by integrating Equation (16) over the energy E of the electron distribution $N_e(E, z)$ and the initial photon energy ϵ as

$$q_{IC}^{tot}(E_{ph}, z) = \int_{E_e^{(min)}}^{E_e^{(max)}} \int_{\epsilon_{min}}^{\epsilon_{max}} N_e(E, z) q_{IC}(\epsilon, E, E_{ph}) d\epsilon dE \,, \tag{18}$$

where the integration limits are $\epsilon_{min} = \epsilon f$ and $\epsilon_{max} = 4\gamma^2 \epsilon_{min}$.

The corresponding luminosity per photon energy of the inverse Compton process is written as

$$L_{IC}(E_{ph}) = \int_V d^3 r E_{ph} q_{IC}^{tot} \,. \tag{19}$$

The volume integral corresponds to the jet region that contains the accelerated electrons.

4.2. Hadron Interactions

While traveling across the jet length, the relativistic jet hadrons (mainly protons) collide with the thermal protons of the jet. The $p-p$ interactions lead to neutral and charged pion production. The first decay to gamma-ray photons is according to the reaction

$$\pi^0 \rightarrow \gamma + \gamma \,. \tag{20}$$

Therefore, the corresponding pion production rate, assuming the relativistic proton distribution discussed above, is written as

$$Q_{\pi^0}(E_\pi, z) = cn(z) K_\pi^{-1} \bar{N}_{\pi^0} \sigma_{pp}^{inel}(E_p) N_p(E_p, z) \,. \tag{21}$$

In the latter expression, $n(z)$ denotes the thermal proton density, $K_\pi \approx 0.17$ is the respective inelasticity, and $\bar{N}_{\pi^0} \approx 1.1$ is the mean number of neutral pions produced per $p-p$ collision.

Assuming that the energy of the produced photons is $E_{ph} < 100$ GeV, it holds

$$Q_\gamma^{(<100\ GeV)}(E_{ph}, z) = 2 \int_{E_\pi^{min}}^{E_\pi^{max}} \frac{Q_{\pi^0}(E_\pi, z)}{\left(E_\pi^2 - m_\pi^2 c^4\right)^{1/2}} dE_\pi \,, \tag{22}$$

where $E_\pi^{min} = E_{ph} + m_\pi^2 c^4/(4E_{ph})$ and $E_\pi^{max} = K_\pi \left(E_p^{max} - m_p c^2\right)$. In the case of $E_{ph} > 100$ GeV, simulations over spectra per $p-p$ collision are implemented [29] and then

$$Q_\gamma^{(>100\ GeV)}(E_{ph}, z) = cn(z) \int_{x_{max}}^1 \frac{dx}{x} N_p\left(\frac{E_{ph}}{x}, z\right) F_\gamma\left(x, \frac{E_{ph}}{x}\right) \sigma_{pp}^{(inel)}\left(\frac{E_{ph}}{x}\right) . \tag{23}$$

The highest portion of the initial energy gained by the photon is $x_{max} = E_{ph}/E_{max}$. Finally, the respective luminosity is given by integrating over the jet volume as

$$L(E_{ph}) = \int_V E_{ph}^2 Q_\gamma(E_{ph}, z) d^3 r = \pi tan^2 \xi \int_{z_0}^{z_{max}} E_{ph}^2 Q_\gamma(E_{ph}, z) z^2 dz \,. \tag{24}$$

This volume corresponds to the acceleration zone.

5. Results and Discussion

In Figure 4, we present the spectral energy distribution emitted from the disk, the companion star, and the jet for our model XRB with the free parameterization of Table 1. The jet region is located at the distance $z = 10^{12}$ cm from the black hole. As can be seen, the synchrotron mechanism is dominant for energies even up to a few GeVs. The peak, however, is provided by the soft X-ray emission of the accretion disk, which is strongly dependent on the mass accretion rate $\dot{M}_{accr}$ and on an effective stellar wind facilitating the process. The disk's IC spectrum provides a smoother transition to the VHE regime, even though it is not distinguishable due to the dominating contribution of the synchrotron mechanism to the SED.

Moreover, the stellar UV emission is eclipsed by the synchrotron component. However, a factor of three in the total stellar luminosity would produce a second distinguishable peak near the respective disk in Figure 4. On the other hand, the inverse comptonization of stellar photons produces a weaker spectrum than that emanating from the disk, as expected from their respective luminosities, even though they cover the same frequency band. Finally,

the hadronic mechanism extends the SED in the ultra-high-energy (UHE) regime. It is worth noting that, given the magnitude of the luminosity and the present sensitivity of the telescopes operating up to 10 TeV, the prospects for such emission detection are limited.

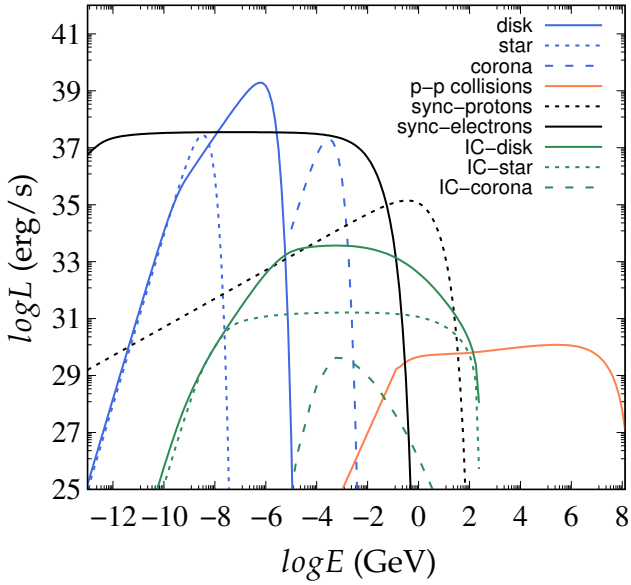

Figure 4. All the contributions to the emitted SED due to thermal (and nonthermal in the case of the corona) (blue), synchrotron (black), and inverse Compton (green) mechanisms, as well as emission due to proton interactions inside the jet (orange). The solid lines represent the most prominent sources of each radiative process.

In the present work, we include also the contribution of the corona, assuming that its radius is $R_c = 30R_g$ (with M_{BH}=10$M_\odot$). The emitted spectrum obeys a power-law distribution with an exponential cutoff at $E_c \approx 100$ keV given by

$$\frac{dn}{d\epsilon} = A\left(\frac{R_c}{\rho}\right)^2 \epsilon^{-p} e^{-\epsilon/E_c}, \tag{25}$$

where $p \approx 1.5$, A denotes a normalization constant and ρ the distance from the compact object. In addition, the respective inverse Compton component of corona emission on jet electrons is plotted in Figure 4. Moreover, several corona-induced mechanisms, such as inverse comptonization of the disk or jet photons, further enhanced by the pair products of $\gamma - \gamma$ interactions, could provide another source of spectral variability.

Given the SED contribution of each mechanism, we investigate the dependence of the total SED on the free parameters employed in addition to the inclination angle and distance of the acceleration zone from the compact object. Figure 5 demonstrates the latter (left panel) and the reduced counterpart due to $\gamma - \gamma$ interactions with colder, ambient photons (right panel). The proton-induced processes, especially the $p - p$ collision rate, are affected mainly by the distance from the black hole due to the jet expansion following its assumed conical geometry. The magnetic field density also drops with the distance, decreasing synchrotron emission by both leptons and hadrons.

For the specific system studied in this work, the estimated radio emission seems to be large compared with observational data from similar XRBs, such as Cygnus X-1 (i.e., $L \geq 2 \times 10^{31}$ erg/s) [30]. This occurs mainly due to the electron distribution and injection rate as well as the maximum electron energy. The latter is determined by the lack of additional electron cooling interactions inside the jet. In Figure 5, we can see that the respective radio emission is positively affected by increasing the distance to the black hole due to the decrease in magnetic field strength and synchrotron cooling. The sub-

equipartition between the magnetic field and plasma is also a reason of insufficient cooling. It was suggested to explain the lack of synchrotron cooling in the AGN jet M87 [31].

In our case, synchrotron losses are the leading force in shaping the relativistic electron distribution and, therefore, the emitted spectrum. However, inverse Compton losses due to interactions with synchrotron emission (synchrotron self-Compton, SSC) are ruled out of our calculations due to the requirement of the particle distribution in order to calculate the emitted synchrotron energy density. Additional IC emission sources, such as the accretion disk or the donor star, have marginally negligible contribution on the total particle cooling rate. Regarding the observations, the synchrotron mechanism was not deemed suitable to explain the flat-radio spectrum component from Cygnus X-1 [30]. Some suggested mechanisms include the optically thin free–free emission from a thermal plasma [32,33] or the combination of synchrotron (or another) mechanism with a thermal component [30].

A possible detection of VHE emission could occur in the lower jet regions, namely, $z \approx 10^8$–10^9 cm. Nonetheless, high photon absorption is also taking place there. As seen from the right panel of Figure 5, the mostly affected energy band is 10–10^4 GeV for $z < 10^{10}$ cm. This region coincides with the VHE regime in which various telescopes are currently operating, such as MAGIC, HESS, Fermi-LAT, and VERITAS [34–37].

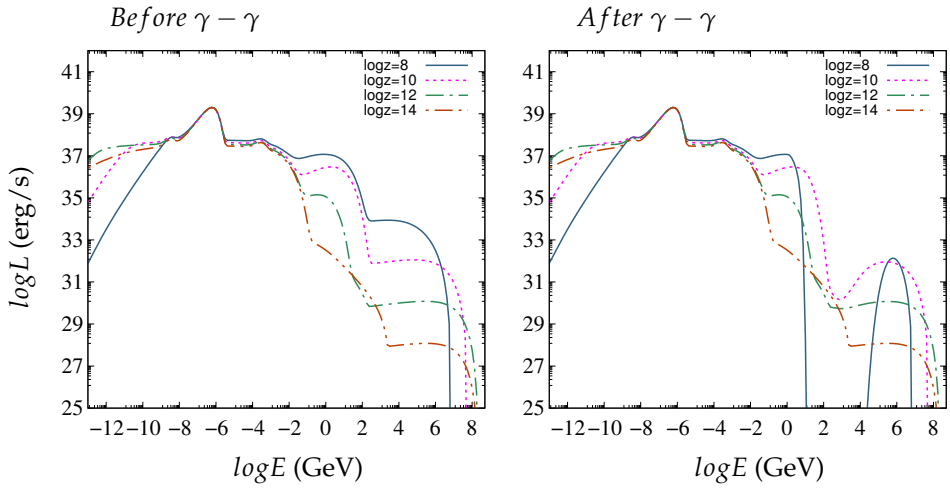

Figure 5. SED dependence on the distance of the jet emission region from the compact object before (**left panel**) and after (**right panel**) engagement with photon clouds from the disk and companion star.

Regarding the hadron-to-lepton ratio α, it impacts the relevant model dynamics between the dominant interactions within the jet boundaries, as shown in Figure 6 (left panel). Lower parameter values strengthen the electron-induced synchrotron component up to 1 GeV, while at the same time, they weaken the proton synchrotron emission and the neutral pion production rate.

The higher acceleration efficiency of the second Fermi mechanism (driven by the parameter η) shifts the produced SED to higher energies, as indicated in the right panel of Figure 6. It should be noted that more intense energy-draining interactions should be able to counter that effect.

Regarding the binary's orientation, a more head-on view of the jet affects positively the predicted SED. This dependence is demonstrated in Figure 7 (left panel). A decrease in the angle between the ejection axis and the line of sight shifts the jet component of the spectrum upwards due to relativistic beaming effects. The reason is that the inclination enters the calculations through Equation (10). We note that, in this case, we do not consider absorption effects. Otherwise, the emitted SED would present a significant variability. We should mention that we calculate the corresponding optical depth seen by a single photon traveling across the path from the emission region to the observer. This makes the emission from lower jet slices depend highly on the orientation.

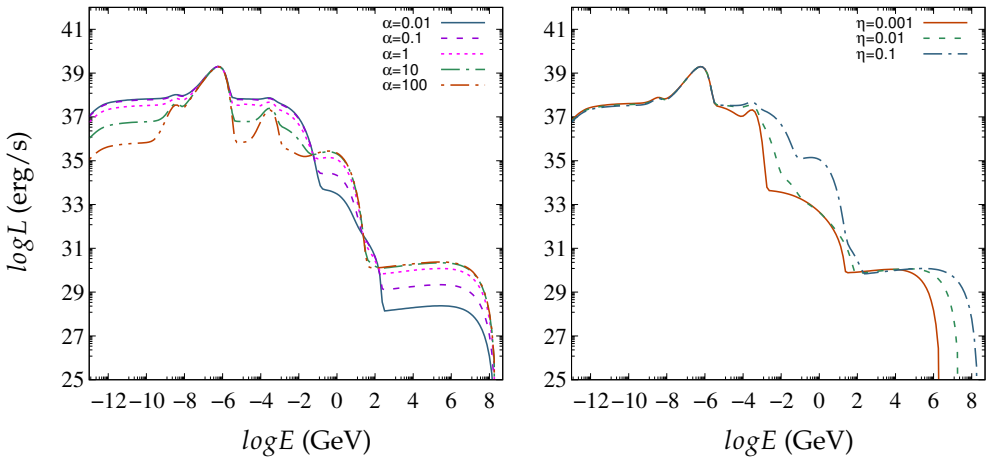

Figure 6. SED dependence on the nature of the jet's content (**left panel**) and shock acceleration efficiency (**right panel**).

The right panel of Figure 7 demonstrates the SED dependence on the length of the acceleration zone through the free parameter $j = z_{max}/z_0$. As we can see, even an extension by two orders of magnitude of the acceleration zone does not significantly impact the jet-produced nonthermal emissions. The reason is related to the fact that the lower jet regions contribute the most to the expected emission due to the higher particle densities and jet compactness. It is worth noting that a semicylindrical jet would be less affected since the drop in particle densities and, thus, the interaction rates would not be as steep.

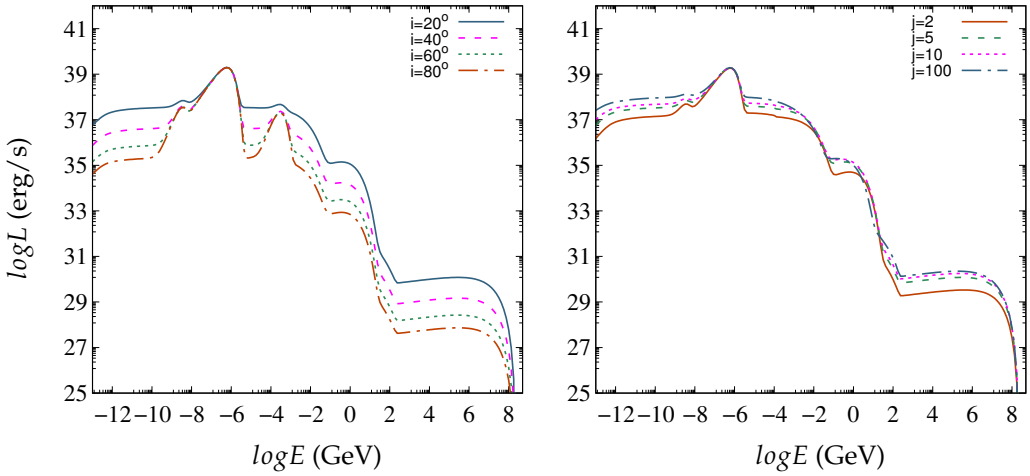

Figure 7. Emitted SED for different views of the incoming jet (**left panel**) and acceleration zone lengths (**right panel**).

Our predictions show increased disk luminosity (i.e., $L_{disk} \approx 10^{39}$ erg/s) compared with other estimations of $L_{disk} \approx 10^{36}$ erg/s [21,38,39]. As shown in Figure 8 (right panel), this is due to the different maximum temperatures and inner disk boundary. The binary system's inclination also impacts the disk luminosity measured by an observer. However, in this case, the deviation from similar calculations in other works would be attributed to the maximum temperature since a decrease of even half an order of magnitude could reproduce these results [40]. It should be noted, however, that the disk modeling is rather simplistic. In our case, the disk is much hotter (i.e., $T_{max} \approx 10^7$ K) and effectively emits from its whole surface, starting from the innermost stable orbit corresponding to a nonrotating black hole (i.e., $R_{in} = 6R_g$). This also reflects on the disk-induced absorption of high-energy gamma rays, which may partially explain the lack of observational data from many well-known XRBs [41–43]. In addition, we consider that the disk is heated only through viscous dissipation. Hence,

irradiation effects [44] of the outer disk regions are not included in the predictions. Contrary to the commonly assumed temperature profile of the disk (i.e., $T \sim R^{-n}$), in this work, we employ the model of Ref. [23], which describes better the boundary conditions near the edge of the disk, close to the black hole, and gives a more realistic temperature transition as the radius grows.

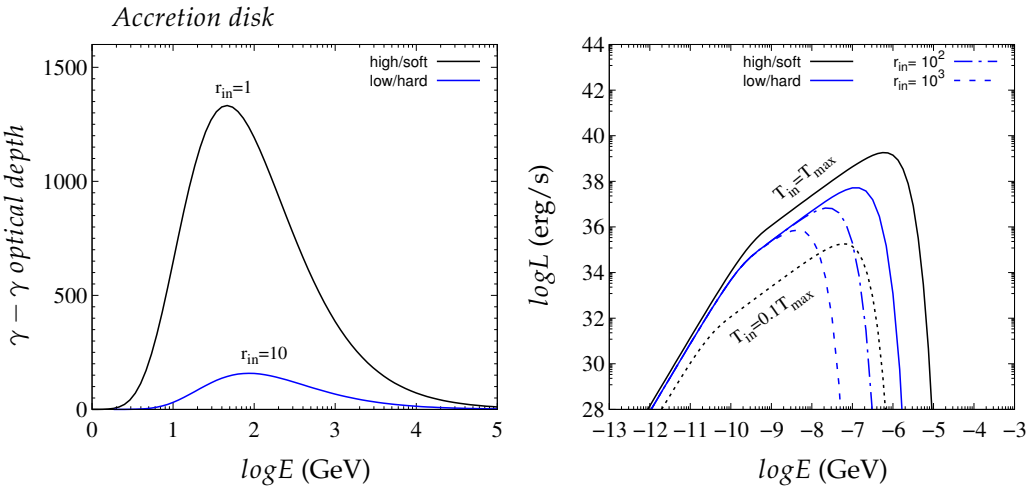

Figure 8. The disk optical depth (**left panel**) and total luminosity (**right panel**) dependence on the inner disk boundary $r_{in} = R_{in}/R_{isco}$, where $R_{isco} = 6R_g$. In the right panel, the impact of the respective temperature T_{in} is also depicted. The black lines (solid and dashed) correspond to $r_{in} = 1$, and the solid blue line to $r_{in} = 10$.

Many BHXRBs experience a spectral transition between two primary states: the high/soft and the low/hard. The first is associated with a thermal, soft X-ray distribution attributed to the accretion disk and possibly a higher-energy tail, as in Cygnus X-1. In this state, the mass accretion rate is comparably significant and the disk extends to the ISCO radius, in agreement with our assumption. The second state introduces the hardening of the X-ray spectrum. It is characterized by a disk truncation to larger radii (i.e., larger than the ISCO radius), thus leaving a void to be filled by an advection-dominated optically thin gas (i.e., ADAF) that constitutes the origin of the system's corona. In addition, this state designates the existence of stable jets accompanied by radio emission detection [45–48].

While considering a system in its low/hard state associated with stable and radiatively active jets, the adopted disk model does not compensate for the disk truncation case. However, we assume a jet acceleration region far from the compact object. Hence, the absorption effects do not impact further the predicted SEDs. As can be seen in the right panel of Figure 8, the disk luminosity decreases accordingly with the disk's inner radius increase. In addition, we demonstrate the dependence of the respective pair-production optical depth on the disk's inner boundary in the left panel of Figure 8. It should be mentioned that the mass accretion rates assumed in obtaining the results of Figure 8 are $\dot{m}_{accr} \approx 0.04$ for the low/hard state and $\dot{m}_{accr} \approx 0.4$ for the high/soft. These values fall under the Eddington regime and justify our choice to employ the thin disk model.

One of our main aims in this work was to investigate the parameterization margins and their impact on the predicted SEDs. We can also discuss additional phenomena that may alter the predicted spectra. The synchrotron emissions of secondary particles, such as the $p - p$ collision products, are negligible compared with lepto-hadrons. Similar is the case of Bremsstrahlung emission. Concerning the electron density distribution, synchrotron losses dominate over inverse Compton scatterings, while protons are mostly affected energy-wise by the jet radius increase with the distance.

A better way to assess our results is the calculation of the respective integral flux from the employed model XRB. For this aim, we consider two separate cases based on the free parameter values of Table 2. The first one (Case A) corresponds to a radiatively efficient jet dominated by leptons, with sufficient particle acceleration output within a lengthy zone of

the jet. The second case (Case B) associates the binary system with a radiatively inactive, hadron-dominated jet inclined almost perpendicularly to our line of sight.

Table 2. Parameterization corresponding to a leptonic (Case A) and a hadronic (Case B) jet. The first constitutes a more effective particle accelerator compared with the second case.

Parameter	Case A	Case B
η	0.1	0.001
α	0.01	100
j	100	2
i	20°	80°

In both cases, the emitted fluxes are presented in the left panel of Figure 9 for an increasing energy threshold (i.e., E_{min}). The incoming disk and stellar fluxes minimize the discrepancy between Cases A and B in the $E_{min} = 10^{-8}$–10^{-5} GeV range, while the corona generates the integral flux peak at $E_{min} = 10^{-4}$–10^{-3} GeV. Otherwise, the flux gap between the two separate cases (i.e., A and B) grows to five orders of magnitude in the remaining part of the extended range. At the same time, the discrepancy in the emission efficiency between the two jets maximizes for $E_{min} = 0.01$ GeV due to the highly accelerated particles' output combined with the synchrotron curve's cutoff. The right panel of Figure 9 compares the emitted photon flux from two identical jets distinguished only by their particle content. Again, the discrepancy is limited to less than two orders of magnitude, while the lepton-dominated jet emits higher, up to 0.1 GeV.

Under these circumstances, the detection of VHE emission from the jet is difficult for $z \geq 10^{12}$ cm unless a substantial increase in $p - p$ collisions occurs due to wind penetration of the jet; see, for example, Ref. [21]. Even accounting for a stellar wind contribution, the particle densities at these jet altitudes (i.e., $z_0 \approx 10^{12}$ cm) are too small to sufficiently be engaged in photon-emitting interactions unless we consider a highly collimated jet at greater distances (adopting a semicylindrical jet model). In order to have a visible impact on our predicted SEDs, the proton density provided by the wind should be at least $n_w \approx 10^8$–10^9 cm^{-3}, which is satisfied in the case of a stellar wind penetrating the jet at the distance $z < 10^{12}$ cm [21]. For greater values of z, the wind density falls under the limit of $n_w \approx 10^8$ cm^{-3}, and the stellar wind contribution becomes marginally negligible.

Even assuming the highest emission case, the integral flux for $E > 100$ GeV is below the established upper flux limits for many well-studied galactic XRBs (i.e., $\Phi < 10^{-12}$–10^{-13} cm^{-2}s^{-1}) [41–43]. On the other hand, emission from lower jet parts is heavily affected by photon absorption. That leaves the jet region at the distance $z = 10^{11}$ cm with the highest probability of emitting detectable VHE gamma-ray fluxes, as seen also in Ref. [40].

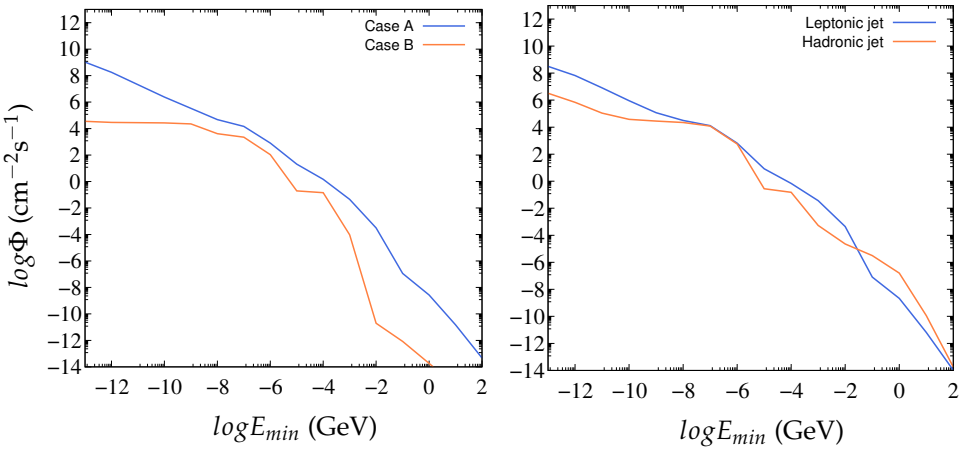

Figure 9. Integral fluxes with increasing energy threshold from our model XRB. The left panel presents two opposite cases corresponding to the free parameters fitting a radiatively efficient jet (Case A) and a relatively inactive jet (Case B). The panel on the right compares a leptonic and a hadronic jet.

6. Summary and Conclusions

Black hole X-ray binaries constitute some of the most intriguing galactic objects with significant multimessenger emission emanating from the extremely hot accretion disk, the black hole's corona, the companion star, and their twin jets. In this work, we attempt to provide predictions of the emitted spectral energy distribution from a standard XRB in our Galaxy (located at the distance $d \approx 2$ kpc) and adjust the model parameterization so as to produce higher detection probabilities through enhanced integral fluxes.

Towards this purpose, we employed a lepto-hadronic model and assumed conic-shaped jets to reproduce the system's synchrotron and inverse Compton spectrum components in addition to the VHE gamma-ray tail. The companion star was assumed to be a very luminous supergiant of type O or B, as is the case of the Cygnus X-1 system. We also consider a typical Shakura–Sunyaev accretion disk that extends from $6R_g$ up to $10^6 R_g$ with a maximum temperature that reaches up to $T_{max} \sim 10^7$ K and emits mostly soft/hard X-rays. We, finally, take into consideration the jet photon absorption effects due to stellar and disk emissions.

For emissions from radio to VHE gamma rays, we find increased integral fluxes emanated from galactic BHXRBs with a more head-on view of a lepton-dominated jet. The shock-induced acceleration occurs preferably at a higher distance from the black hole to avoid photon absorption effects. Optimally, this zone terminates at $z_{max} > 10z_0$ to include a more significant portion of the jet. Under these conditions, acceleration zones extending higher than $10z_0$ would not impact the produced integral flux appreciably because the gamma-ray photon production increases only marginally above this region. We found that the efficiency of acceleration does not have a significant impact on VHE gamma-ray detection. However, it boosts lower emissions above hard X-rays, where the dominant jet emission mechanisms remaining are the synchrotron radiation and inverse comptonization of low-energy photons. Finally, absorption effects due to disk and stellar emissions create a gap in the spectrum in the range of 10–10^4 GeV, mainly concerning the lower jet regions, where the photon production mechanisms reach their highest efficiency. Most current telescopes operate at energies corresponding to this gap, making absorption due to a highly heated accretion disk a possible explanation for the lack of relevant observations in this energy range.

Author Contributions: Conceptualization, T.P. and O.K.; methodology, T.P.; software, T.P.; validation, O.K. and I.S.; formal analysis, T.P.; investigation, T.P.; resources, I.S.; data curation, O.K.; writing—original draft preparation, T.P.; writing—review and editing, O.K.; visualization, T.P.; supervision, I.S.; project administration, I.S. All authors have read and agreed to the published version of the manuscript.

Funding: This research received no external funding.

Data Availability Statement: The datasets generated during and/or analyzed in the present study are available upon request from the corresponding author.

Acknowledgments: The authors T.P. and O.K. wish to acknowledge funding by the OPRA Association (Tel Aviv, Israel) project No. 83241/ELKE University of Ioannina, Greece.

Conflicts of Interest: The authors declare no conflict of interest.

References

1. Blandford, R.D.; Znajek, R.L. Electromagnetic extraction of energy from Kerr black holes. *Mon. Not. R. Astron. Soc* **1977**, *179*, 433–456. [CrossRef]
2. Blumenthal, G.R.; Gould, R.J. Bremsstrahlung, Synchrotron Radiation, and Compton Scattering of High-Energy Electrons Traversing Dilute Gases. *Rev. Mod. Phys.* **1970**, *42*, 237–271. [CrossRef]
3. Atoyan, A.M.; Aharonian, F.A. Modelling of the non-thermal flares in the Galactic microquasar GRS 1915+105. *Mon. Not. R. Astron. Soc.* **1999**, *302*, 253–276.
4. Markoff, S.; Falcke, H.; Fender, R. A jet model for the broadband spectrum of XTE J1118+480—Synchrotron emission from radio to X-rays in the Low/Hard spectral state. *Astron. Astrophys.* **2001**, *372*, L25–L28. [CrossRef]

5. Bosch-Ramon, V.; Romero, G.E.; Paredes, J.M. A broadband leptonic model for gamma-ray emitting microquasars. *Astron. Astrophys.* **2006**, *447*, 263–276. [CrossRef]
6. Khangulyan, D.; Aharonian, F.; Bosch-Ramon, V. On the formation of TeV radiation in LS 5039. *Mon. Not. R. Astron. Soc.* **2007**, *383*, 467–478.
7. Smponias, T.; Kosmas, T.S. Dynamical and radiative simulations of γ-ray jets in microquasars. *Mon. Not. R. Astron. Soc.* **2013**, *438*, 1014–1026.
8. Kosmas, O.; Smponias, T. Simulations of Gamma-Ray Emission from Magnetized Microquasar Jets. *Adv. High Energy Phys.* **2018**, *2018*, 9602960. [CrossRef]
9. Romero, G.E.; Torres, D.F.; Kaufman Bernadó, M.M.; Mirabel, I.F. Hadronic gamma-ray emission from windy microquasars. *Astron. Astrophys.* **2003**, *410*, L1–L4. [CrossRef]
10. Romero, G.E.; Okazaki, A.T.; Orellana, M.; Owocki, S.P. Accretion vs. colliding wind models for the gamma-ray binary LS I +61 303: An assessment. *Astron. Astrophys.* **2007**, *474*, 15–22. [CrossRef]
11. Reynoso, M.M.; Romero, G.E. Magnetic field effects on neutrino production in microquasars. *Astron. Astrophys.* **2009**, *493*, 1–11. [CrossRef]
12. King, A.R. Accretion rates and beaming in ultraluminous X-ray sources. *Mon. Not. R. Astron. Soc. Lett.* **2008**, *385*, L113–L115. [CrossRef]
13. Abramowicz, M.A.; Fragile, P.C. Foundations of Black Hole Accretion Disk Theory. *Living Rev. Relativ.* **2013**, *16*, 1. [CrossRef]
14. Shakura, N.I.; Sunyaev, R.A. Black holes in binary systems. Observational appearance. *Astron. Astrophys.* **1973**, *24*, 337–355.
15. Narayan, R.; Yi, I. Advection-dominated Accretion: Underfed Black Holes and Neutron Stars. *Astrophys. J.* **1995**, *452*, 710.
16. Bardeen, J.M.; Press, W.H.; Teukolsky, S.A. Rotating Black Holes: Locally Nonrotating Frames, Energy Extraction, and Scalar Synchrotron Radiation. *Astrophys. J.* **1972**, *178*, 347–370. [CrossRef]
17. Papavasileiou, T.; Kosmas, O.; Sinatkas, I. Simulations of Neutrino and Gamma-Ray Production from Relativistic Black-Hole Microquasar Jets. *Galaxies* **2021**, *9*, 67. [CrossRef]
18. Papavasileiou, T.; Kosmas, O.; Sinatkas, I. Relativistic Magnetized Astrophysical Plasma Outflows in Black-Hole Microquasars. *Symmetry* **2022**, *14*, 485. [CrossRef]
19. Papavasileiou, T.V.; Papadopoulos, D.A.; Kosmas, T.S. Astrophysical magnetohydrodynamical outflows in the extragalactic binary system LMC X-1. *J. Phys. Conf. Ser.* **2021**, *1730*, 012138. [CrossRef]
20. Abdo, A.A.; Ackermann, M.; Ajello, M.; Atwood, W.B.; Axelsson, M.; Baldini, L.; Ballet, J.; Barbiellini, G.; Bastieri, D.; Baughman, B.M.; et al. Fermi/LAT observations of LS 5039. *Astrophys. J.* **2009**, *706*, L56. [CrossRef]
21. Pepe, C.; Vila, G.S.; Romero, G.E. Lepto-hadronic model for the broadband emission of Cygnus X-1. *Astron. Astrophys.* **2015**, *584*, A95. [CrossRef]
22. Pringle, J.E. Accretion discs in astrophysics. *Annu. Rev. Astron. Astrophys.* **1981**, *19*, 137–162. [CrossRef]
23. Cerutti, B.; Dubus, G.; Malzac, J.; Szostek, A.; Belmont, R.; Zdziarski, A.A.; Henri, G. Absorption of high-energy gamma rays in Cygnus X-3. *Astron. Astrophys.* **2011**, *529*, A120. [CrossRef]
24. Gould, R.G.; Schréder, G.P. Pair Profuction in Photon-Photon Collisions. *Phys. Rev.* **1967**, *155*, 1404. [CrossRef]
25. Böttcher, M.; Dermer, C.D. Photon-Photon Absorption of Very High Energy Gamma Rays from Microquasars: Application to LS 5039. *Astrophys. J.* **2005**, *634*, L81–L84. [CrossRef]
26. Reynoso, M.M.; Carulli, A.M. On the possibilities of high-energy neutrino production in the jets of microquasar SS433 in light of new observational data. *Astropart. Phys.* **2019**, *109*, 25–32. .: 10.1016/j.astropartphys.2019.02.003. [CrossRef]
27. Gliozzi, M.; Bodo, G.; Ghisellini, G. The bulk kinetic power of the jets of GRS 1915+105. *Mon. Not. R. Astron. Soc.* **1999**, *303*, L37–L40.
28. Cao, X.; Lai, D. Jet production in black hole X-ray binaries and active galactic nuclei: Mass feeding and advection of magnetic fields. *Mon. Not. R. Astron. Soc.* **2019**, *485*, 1916–1923.
29. Kelner, S.R.; Aharonian, F.A.; Bugayov, V.V. Energy spectra of gamma rays, electrons, and neutrinos produced at proton-proton interactions in the very high energy regime. *Phys. Rev. D* **2006**, *74*, 034018. [CrossRef]
30. Fender, R.P.; Pooley, G.G.; Durouchoux, P.; Tilanus, R.P.J.; Brocksopp, C. The very flat radio-millimetre spectrum of Cygnus X-1. *Mon. Not. R. Astron. Soc.* **2000**, *312*, 853–858.
31. Heinz, S.; Begelman, M.C. Analysis of the Synchrotron Emission from the M87 Jet. *Astrophys. J.* **1997**, *490*, 653. [CrossRef]
32. Shang, H.; Lizano, S.; Glassgold, A.; Shu, F. Free-free Radio Emission from Young Stellar Objects. *Astrophys. J.* **2004**, *612*, L69–L72. [CrossRef]
33. Ohmura, T.; Machida, M.; Nakamura, K.; Kudoh, Y.; Asahina, Y.; Matsumoto, R. Two-Temperature Magnetohydrodynamics Simulations of Propagation of Semi-Relativistic Jets. *Galaxies* **2019**, *7*, 14. [CrossRef]
34. Albert, J.; Aliu, E.; Anderhub, H.; Antoranz, P.; Armada, A.; Asensio, M.; Baixeras, C.; Barrio, J.A.; Bartelt, M.; Bartko, H.; et al. Observation of Gamma Rays from the Galactic Center with the MAGIC Telescope. *Astrophys. J.* **2006**, *638*, L101. [CrossRef]
35. Bolmont, J.; Corona, P.; Gauron, P.; Ghislain, P.; Goffin, C.; Guevara Riveros, L.; Huppert, J.F.; Martineau-Huynh, O.; Nayman, P.; Parraud, J.M.; et al. The camera of the fifth H.E.S.S. telescope. Part I: System description. *Nucl. Instrum. Methods Phys. Res. A* **2014**, *761*, 46–57. [CrossRef]
36. Acero, F.; Ackermann, M.; Ajello, M.; Albert, A.; Atwood, W.B.; Axelsson, M.; Baldini, L.; Ballet, J.; Barbiellini, G.; Bastieri, D.; et al. Fermi large area telescope third source catalog. *Astrophys. J. Suppl. Ser.* **2015**, *218*, 23. [CrossRef]

37. Acciari, V.A.; Aliu, E.; Arlen, T.; Aune, T.; Beilicke, M.; Benbow, W.; Bradbury, S.M.; Buckley, J.H.; Bugaev, V.; Byrum, K.; et al. Veritas observations of the TeV binary LS I +61° 303 during 2008–2010. *Astrophys. J.* **2011**, *738*, 3. [CrossRef]
38. Vila, G.S.; Romero, G.E.; Casco, N.A. An inhomogeneous lepto-hadronic model for the radiation of relativistic jets—Application to XTE J1118+480. *Astron. Astrophys.* **2012**, *538*, A97. [CrossRef]
39. Kantzas, D.; Markoff, S.; Beuchert, T.; Lucchini, M.; Chhotray, A.; Ceccobello, C.; Tetarenko, A.J.; Miller-Jones, J.C.A.; Bremer, M.; Garcia, J.A.; et al. A new lepto-hadronic model applied to the first simultaneous multiwavelength data set for Cygnus X–1. *Mon. Not. R. Astron. Soc.* **2020**, *500*, 2112–2126.
40. Papavasileiou, T.V.; Kosmas, O.T.; Sinatkas, I. Prediction of gamma-ray emission from Cygnus X-1, SS 433, and GRS 1915+105 after absorption. *Astron. Astophys.* **2023**, *673*, A162. [CrossRef]
41. Schüssler, F.; Bordas, P.; Chadwick, P.M.; Dickinson, H.; Ernenwein, J.P. Simultaneous H.E.S.S. and RXTE observations of the microquasars GRS 1915+105, Circinus X-1 and V4641 Sgr. *arXiv* **2015**, arXiv:1509.03039. [CrossRef]
42. Ahnen, M.; Ansoldi, S.; Antonelli, L.; Arcaro, C. Search for very high-energy gamma-ray emission from the microquasar Cygnus X-1 with the MAGIC telescopes. *Mon. Not. R. Astron. Soc.* **2017**, *472*, 3474–3485. [CrossRef]
43. Ahnen, M.L.; Ansoldi, S.; Antonelli, L.A.; Arcaro, C.; Babi´c, A.; Banerjee, B.; Bangale, P.; Barres de Almeida, U.; Barrio, J. A.; Becerra González, J.; et al. Constraints on particle acceleration in SS433/W50 from MAGIC and H.E.S.S. observations. *Astron. Astrophys.* **2018**, *612*, A14. [CrossRef]
44. Maitra, D.; Markoff, S.; Brocksopp, C.; Noble, M.; Nowak, M.; Wilms, J. Constraining jet/disc geometry and radiative processes in stellar black holes XTE J1118+480 and GX 339–4. *Mon. Not. R. Astron. Soc.* **2009**, *398*, 1638–1650.
45. Esin, A.A.; McClintock, J.E.; Narayan, R. Advection-Dominated Accretion and the Spectral States of Black Hole X-Ray Binaries: Application to Nova Muscae 1991. *Astrophys. J.* **1997**, *489*, 865. [CrossRef]
46. Gierliński, M.; Zdziarski, A.A.; Poutanen, J.; Coppi, P.S.; Ebisawa, K.; Johnson, W.N. Radiation mechanisms and geometry of Cygnus X-1 in the soft state. *Month. Not. R. Astron. Soc.* **1999**, *309*, 496–512.
47. Done, C.; Gierliński, M.; Kubota, A. Modelling the behaviour of accretion flows in X-ray binaries. *Astron. Astrophys. Rev.* **2007**, *15*, 1–66. [CrossRef]
48. Makishima, K.; Takahashi, H.; Yamada, S.; Done, C.; Kubota, A.; Dotani, T.; Ebisawa, K.; Itoh, T.; Kitamoto, S.; Negoro, H.; et al. Suzaku Results on Cygnus X-1 in the Low/Hard State. *Publ. Astron. Soc. Jpn.* **2008**, *60*, 585–604.